

RobustSpring: Benchmarking Robustness to Image Corruptions for Optical Flow, Scene Flow and Stereo

Jenny Schmalfuss*¹Victor Oei*²Lukas Mehl¹Madlen Bartsch²Shashank Agnihotri³Margret Keuper^{3,4}Andrés Bruhn¹

Figure 1. RobustSpring is a novel image corruption benchmark for optical flow, scene flow and stereo. It evaluates 20 image corruptions including blurs, color changes, noises, quality degradations, and weather, applied to stereo video data from [43]. For comprehensive robustness evaluations on all three tasks, RobustSpring’s image corruptions are integrated in time, stereo and depth where applicable.

Abstract

Standard benchmarks for optical flow, scene flow, and stereo vision algorithms generally focus on model accuracy rather than robustness to image corruptions like noise or rain. Hence, the resilience of models to such real-world perturbations is largely unquantified. To address this, we present RobustSpring, a comprehensive dataset and benchmark for evaluating robustness to image corruptions for optical flow, scene flow, and stereo models. RobustSpring applies 20 different image corruptions, including noise, blur, color changes, quality degradations, and weather distortions, in a time-, stereo-, and depth-consistent manner to the high-resolution Spring dataset, creating a suite of 20,000 corrupted images that reflect challenging conditions. RobustSpring enables comparisons of model robustness via a new corruption robustness metric. Integration with the Spring benchmark enables public two-axis evaluations of both accuracy and robustness. We benchmark a curated selection of initial models, observing that accurate models are not necessarily robust and that robustness varies widely by corruption type. RobustSpring is a new computer vision benchmark at spring-benchmark.org that treats robustness as a first-class citizen to foster models that combine accuracy with resilience.

1. Introduction

Optical flow, scene flow, and stereo vision algorithms estimate dense correspondences and enable real-world applications like robot navigation [34, 40, 80], video processing [44], structure-from-motion [38, 50], medical image registration [47] or surgical assistance [51, 56]. While estimation quality continuously improves on accuracy-driven benchmarks [5, 7, 10, 12, 18, 43, 45, 55, 57, 62], their robustness to real-world visual corruptions like sensor noise or compression artifacts is rarely systematically assessed. This lack of systematic assessment is problematic, as better accuracy does not necessarily translate to improved robustness and can even harm model robustness [60, 71]. Though image data in KITTI [45], Sintel [12] or Spring [43] comes with degradations like motion blurs, depth-of-field or brightness changes, they result from real-world data capture or efforts to increase data realism, but were not included to systematically study model predictions under image corruptions. Broad corruption-robustness studies as they ex-

*Equal contribution.

¹University of Stuttgart, VIS-CV. first.last@vis.uni-stuttgart.de

²University of Stuttgart, SimTech.

³University of Mannheim.

⁴Max-Planck-Institute for Informatics, Saarland Informatics Campus.

ist for for image classification [21, 48], 3D object detection [32, 46] or monocular depth estimation [30] are rare for dense-correspondence tasks, where studies are limited to specific degradations like weather [61] or low-light [82]. This not only leaves uncertainty about the reliability of dense matching algorithms in real-world scenarios. It also prevents systematic efforts to improve their robustness.

To enable systematic studies on the image corruption robustness of optical flow, scene flow, and stereo, we propose the *RobustSpring* dataset. Based on Spring [43], it jointly benchmarks the robustness of all three tasks on corrupted stereo videos. While prior image corruptions affect the monocular 2D or 3D space [21, 30, 46], RobustSpring’s image corruptions are integrated in *time*, *stereo* and *depth* and thus tailored to dense matching tasks. A principled corruption robustness metric and public benchmark website make RobustSpring the first systematic tool to evaluate and improve dense matching robustness to image corruptions.

Contributions. Fig. 1 gives an overview of RobustSpring. In summary, we make the following contributions:

- (1) *Tailored image corruptions.* RobustSpring is the first image corruption dataset for optical flow, scene flow and stereo. It integrates 20 corruptions for blurs, noises, tints, artifacts, and weather in time, stereo, and depth.
- (2) *Corruption robustness metric.* We propose a corruption robustness metric, based on Lipschitz continuity, which subsamples the clean-corrupted prediction difference and disentangles robustness and accuracy.
- (3) *Benchmark functionality.* RobustSpring’s standardized evaluation enables community-driven robustness comparisons of dense matching models. Public robustness benchmarking can be integrated with Spring’s website.
- (4) *Initial robustness evaluation.* We benchmark eight optical flow, two scene flow and six stereo models. All models are corruption sensitive, which reveals concealed robustness deficits on dense matching models.

Intended Use. RobustSpring is not a fine-tuning dataset, but a benchmark of how dense matching models generalize to *unseen* image corruptions. It seeks to foster robustness research and, simultaneously, helps assess real-world applicability of models. Hence, it is essential to tie RobustSpring to an existing accuracy benchmark like Spring, as this minimizes the robustness evaluation hurdle for researchers.

2. Related Work

While the quality of optical flow, scene flow and stereo models advanced for over three decades, their robustness recently regained attention as result of brittle deep learning generalization [53, 60]. We review robustness in dense-matching, particularly image corruptions and metrics.

Robustness in Dense Matching. Robustness research for

optical flow, scene flow, and stereo models often focuses on *adversarial attacks*, which quantify prediction errors for optimized image perturbations. Most attacks are for optical flow [4, 33, 53, 60, 61, 63, 77] rather than stereo [11, 74] and scene flow [37, 72]. As remedies to adversarial vulnerability [1–3, 9, 63] may be overcome through specialized optimization [58], another line of robustness research considers unoptimized data shifts. Those come in two flavors: *generalization across datasets*, and *robustness to image corruptions*. Dense matching models typically report generalization [23, 36, 42, 69, 70, 76] to several datasets, which span synthetic [5, 7, 8, 12, 15, 17, 35, 39, 43, 54, 55] and real-world data [18, 31, 45, 57, 62], often in automotive contexts. While some datasets contain image corruptions, *e.g.* motion blur, depth of field, fog, noise or brightness changes [12, 43, 45, 66], they do not systematically assess corruption robustness. Yet, in the wild, robustness to image corruptions is crucial. For optical flow, systematic low light [82] and weather datasets [59, 61] exist, and [63, 78] apply 2D image corruptions [7, 21] to optical flow data. Beyond these isolated works on optical flow, no systematic image-corruption study before RobustSpring spans all three dense matching tasks and includes scene flow or stereo.

Robustness to Image Corruptions. Popularized by 2D common corruptions [21], the field of image corruption robustness rapidly expanded from classification [21, 48] to depth estimation [30], 3D object detection [32, 46] and semantic segmentation [32]. Conceptually, corruptions were extended to the 3D space [30], LiDAR [32], procedural rendering [16] and optical flow [78], but none have been tailored to the depth-, stereo-, and time-dependent setup of dense matching with optical flow, scene flow and stereo.

Robustness Metrics and Benchmarks. Most robustness metrics for dense matching differ by whether they utilize ground truth [4, 53, 78] or not [59–61]. However, multiple works [60, 68, 71] evidence that robustness and accuracy are competing qualities whose quantification should not be mixed, which informs our robustness metric. RobustSpring is the first *robustness* benchmark for three dense-matching tasks, and joins prior benchmarks for optical flow [6], disparity estimation [5] and classification [14, 29, 67]

3. RobustSpring Dataset and Benchmark

RobustSpring is a large, novel, image corruption dataset for optical flow, scene flow, and stereo. Below, we describe how we build on Spring’s stereo video dataset and augment its frames with diverse image corruptions integrated in time, stereo, and depth, how we evaluate robustness to image corruptions, and use it to benchmark algorithm capabilities.

Spring Data. Spring [43] is a high-resolution benchmark and dataset with rendered stereo sequences. It is the ideal



Figure 2. RobustSpring’s image corruptions on a single image.

	Color			Blur			Noise			Qual		Weather								
Property	Brightness	Contrast	Saturate	Defocus	Gaussian	Glass	Motion	Zoom	Gaussian	Impulse	Speckle	Shot	Pixelate	JPEG	Elastic	Spatter	Frost	Snow	Rain	Fog
Time-cons.	✓	✓	✓	✓	✓	✓	✓	✓	-	-	-	-	✓	✓	✓	✓	✓	✓	✓	✓
Stereo-cons.	✓	✓	✓	✓	✓	-	-	✓	-	-	-	-	✓	✓	-	-	-	✓	✓	✓
Depth-cons.	-	-	-	-	-	-	✓	-	-	-	-	-	-	-	-	-	-	✓	✓	✓
SSIM	0.70	0.70	0.72	0.70	0.70	0.73	0.75	0.70	0.20	0.20	0.20	0.22	0.70	0.70	0.70	0.72	0.73	0.70	0.70	0.71

Table 1. Overview of RobustSpring corruptions, whether they are implemented in a time, stereo and depth consistent manner, and their resulting visual changes w.r.t. the original images as SSIM.

base for an image corruption dataset as its detailed renderings permit image alterations of varying granularity – from removing detail by blurring to adding detail via weather. Being a benchmark, Spring has a public training and closed test split, which withholds ground truth for optical flow, disparity, and extrinsic camera parameters. Because our robustness benchmark shall complement accuracy analyses, we use the 2000 Spring test frames, two per stereo camera. For image corruptions with time, stereo, and depth consistency, however, we require the extrinsic camera parameters and depths that are withheld. Thus, we estimate extrinsics using COLMAP 3.8 and depths as $Z = \frac{f_x \cdot B}{d}$, with focal length f_x , baseline length B and stereo disparities d , estimated via MS-RAFT+ [26, 27]. Estimation also prevents data leakage and maintains ground truth confidentiality.

3.1. Corruption Dataset Creation

RobustSpring corrupts the Spring test frames via 20 diverse image corruptions, summarized in Fig. 2 and Tab. 1. Below, we describe the image corruption types, their new consistencies, their implementation, and their severity levels.

Corruption Types. In RobustSpring, we consider the five

image corruption types from [21]: color, blur, noise, quality, and weather. Color simulates different lighting conditions and camera settings, including brightness, contrast, and saturation. Blur acts like focus and motion artifacts, including defocus, Gaussian, glass, motion, and zoom blur. Noise represents sensor errors and ambiance, including Gaussian, impulse, speckle, and shot noise. Quality distortions are lossy compressions and geometric distortions, including pixelation, JPEG, and elastic transformations. Weather enacts outdoor conditions, including spatter, frost, snow, rain, and fog. All corruptions are on a single frame in Fig. 2.

Corruption Consistencies. To increase the realism of these 20 corruptions for dense matching models, we extend their definition to time, stereo, and depth: *Time consistent* corruptions are smooth over time on *one* camera, e.g. frost on a camera lens, which differs per stereo camera. *Stereo consistent* corruptions equally influence both stereo cameras, e.g. brightness changes affect the cameras to the same extent. *Depth consistent* corruptions are integrated into the 3D scene, e.g. snowflakes falling along a trajectory in the 3D space, rendered into the camera view. Tab. 1 summarizes the consistencies we added to 16 of our 20 corruptions. Note that depth-aware motion blur is not stereo-consistent because it depends on the specific camera view.

Corruption Implementation. Though most corruptions are loosely based on [21], our corruption consistencies requires multiple adaptations. Furthermore, we employ specialized techniques for highly consistent effects, i.e. motion blur, elastic transform, snow, rain and fog. We adapt implementations from [21], modify glass blur, zoom blur, frost and pixelation to accommodate higher resolutions and non-square images, and adjust frost, glass blur, and spatter for consistency across video scenes. Motion blur is based on [81] and adds camera-induced motion with clean optical flow estimates. Elastic transform uses PyTorch’s transforms package to create a see-through water-like effect, changing object morphology with smooth frame transitions. For snow and rain, we expand [61]’s two-step 3D particle rendering to multi-step particle trajectories and stereo views, change from additive-blending to order-independent alpha blending [41], and include global illumination [19]. To augment the large-scale Spring data, we improve its performance via more effective particle generation and parallel processing. Fog is based on the Koschmieder model following [73]. Full implementation details are in Appendix B.2.

Corruption Severity. Prior works [21, 30, 32, 46, 48] defined corruptions with several levels of severity. Here we opt for one severity per corruption, because evaluating one scene flow model on all 20 corruptions already produces 2.1 TB of raw data – 1.2 GB after subsampling, cf. Sec. 3.2. More severity levels would overburden the evaluation resources of RobustSpring benchmark users. To

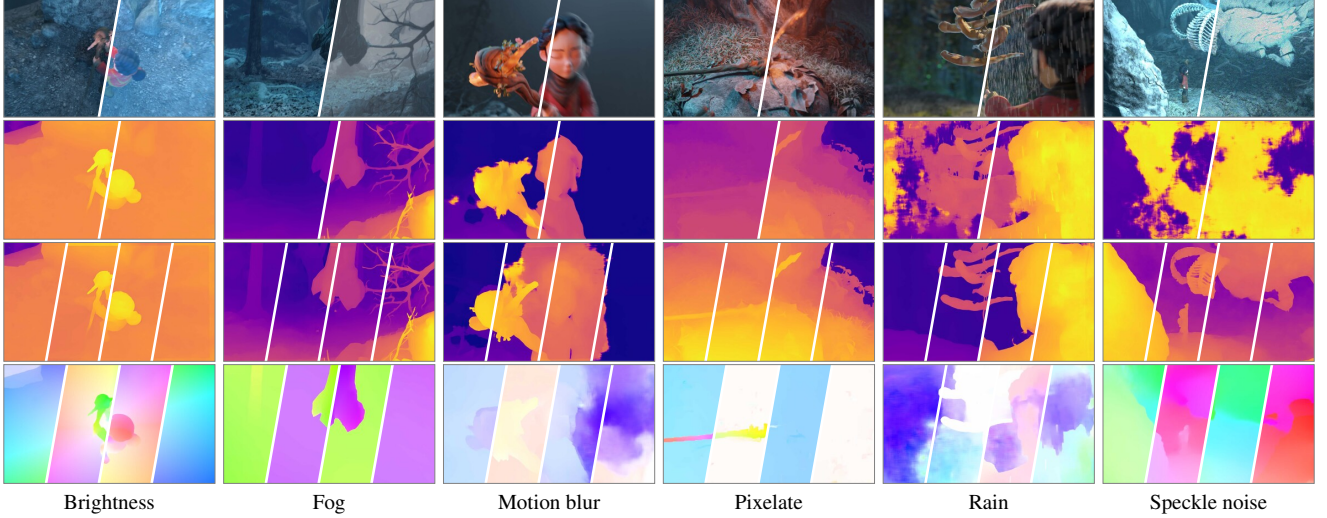


Figure 3. RobustSpring example frames. The first row shows clean and corrupted images. The second row shows the left and right disparity maps predicted with LEA Stereo [13]. The third row shows the target disparities for forward left, backward left, forward right, and backward right directions from M-FUSE [42]. The fourth row shows optical flow estimates for forward left, backward left, forward right, and backward right from RAFT [69]. All disparities and flows are computed on the corrupted dataset, see Fig. A1 in the Supplementary for additional frames.

balance severity across corruptions, we tune their hyperparameters until the image SSIM reaches a defined threshold. We generally use $\text{SSIM} \geq 0.7$, and, because the SSIM is less sensitive to blurs than noises [22], $\text{SSIM} \geq 0.2$ for noises for visually similar artifact strengths. Final SSIMs are in Tab. 1.

3.2. Robustness Evaluation Metric

With various corruption types, we need a metric to quantify model robustness to these variations. In the following, we motivate and derive a ground-truth-free robustness metric for dense matching, introduce subsampling for efficiency, and discuss strategies for joint rankings over corruptions.

Robustness Metric Concepts. For dense matching, robustness to corruptions is undefined. Metrics exist for adversarial robustness, using the distance between corrupt prediction and either (i) ground-truth [4, 53] or (ii) clean prediction [59–61]. The latter is preferred for two reasons: First, (i)’s ground-truth comparisons mix accuracy and robustness, which are competing model qualities [60, 68, 71] that should be separate. This competition is intuitive: A model that always outputs the same value is as robust as inaccurate. Likewise, an accurate model varies for any input change and thus is not robust. Second, (ii) separates robustness from accuracy and builds on an established mathematical concept for system robustness [20, 49]: the Lipschitz constant L^c . It defines robust models as those whose prediction f is similar on clean and corrupt image I and I^c , relative to their difference. For dense matching, it reads

$$L^c = \frac{\|f(I) - f(I^c)\|}{\|I - I^c\|}. \quad (1)$$

This robustness formulation is preferable for real-world applications that demand stable scene estimations *despite* corruptions like snow.

Corruption Robustness Metric. Based on Eq. (1), we quantify model robustness to corruptions. Because RobustSpring’s corrupt images I^c deviate from their clean counterparts I by a similar amount, *cf.* SSIM equalization in Sec. 3.1, we omit the denominator in Eq. (1) and define *corruption robustness* as distance between clean $f(I)$ and corrupted $f(I^c)$ predictions with distance metric M :

$$R_M^c = M[f(I), f(I^c)]. \quad (2)$$

For similarity to Spring’s evaluation, we use corruption robustness with various metrics M , reporting R_{EPE}^c , R_{1px}^c and R_{FI}^c for optical and scene flow, and R_{1px}^c , R_{Abs}^c and R_{D1}^c for stereo. Interestingly, our EPE-based corruption robustness

$$R_{\text{EPE}}^c = \text{EPE}[f(I), f(I^c)] = \frac{1}{|\Omega|} \sum_{i \in \Omega} \|f_i(I) - f_i(I^c)\|, \quad (3)$$

on image domain Ω is a generalization of optical-flow adversarial robustness [60] to dense matching and corruptions.

Metric Subsampling. For a benchmark, users should upload robustness results to a web server. To this end, we evaluate on a reduced pixel set by refining Spring’s original subsampling strategy, which retains about 1% of the full data. First, we additionally subsample the set of full-resolution Hero-frames, leaving 0.95%, and then apply 20-fold subsampling, ultimately keeping 0.05% of the full data.

		GMFlow			MS-RAFT+			FlowFormer			GMA			SPyNet			RAFT			FlowNet2			PWCNet		
		R_{EPE}^c	R_{1px}^c	R_{FI}^c	R_{EPE}^c	R_{1px}^c	R_{FI}^c	R_{EPE}^c	R_{1px}^c	R_{FI}^c	R_{EPE}^c	R_{1px}^c	R_{FI}^c	R_{EPE}^c	R_{1px}^c	R_{FI}^c	R_{EPE}^c	R_{1px}^c	R_{FI}^c	R_{EPE}^c	R_{1px}^c	R_{FI}^c	R_{EPE}^c	R_{1px}^c	R_{FI}^c
Color	Brightness	0.33	3.31	1.12	0.33	2.88	1.02	0.68	2.82	1.05	0.36	3.22	1.04	2.72	14.67	8.91	0.92	3.49	1.61	0.45	3.16	1.05	1.04	7.38	3.00
	Contrast	0.46	6.71	1.71	0.87	6.69	3.24	0.93	5.48	1.96	0.68	6.43	2.20	8.23	38.90	27.23	1.32	5.73	2.64	1.87	9.26	4.74	2.98	30.07	7.42
	Saturate	0.34	3.30	0.96	0.34	2.87	1.03	0.42	2.39	0.88	0.43	3.47	1.18	3.36	17.34	11.31	0.93	3.33	1.47	0.51	3.40	1.10	1.21	9.92	3.68
Blur	Defocus	0.53	6.17	1.45	0.51	4.01	1.47	0.55	3.85	1.19	0.56	5.02	2.01	0.57	10.16	1.36	1.03	4.70	2.07	0.53	3.35	1.06	0.98	6.51	2.78
	Gaussian	0.66	7.77	1.88	0.58	4.45	1.63	0.63	4.32	1.37	0.62	5.48	2.22	0.76	15.44	2.12	1.10	5.12	2.26	0.60	4.05	1.27	1.11	7.72	3.09
	Glass	0.85	20.87	1.82	0.53	4.45	1.37	0.64	4.04	1.17	0.61	5.60	1.91	0.75	16.94	1.36	1.05	5.13	1.97	0.50	3.12	0.96	0.91	5.96	2.47
	Motion	1.34	18.35	7.51	1.31	14.06	6.16	1.35	14.03	5.77	1.19	14.40	6.18	2.32	19.55	10.05	2.06	14.33	6.35	1.60	14.07	6.47	1.95	16.25	7.47
	Zoom	1.88	35.80	9.90	1.81	21.84	7.13	1.66	22.72	6.77	1.54	23.17	7.16	4.82	46.67	28.37	3.14	22.80	7.61	2.36	24.63	9.04	3.52	50.33	15.64
Noise	Gaussian	4.70	57.95	21.67	5.70	35.74	22.12	6.56	27.83	18.30	2.81	24.70	12.96	2.22	42.23	14.88	7.43	27.92	18.99	1.33	11.24	5.06	2.79	26.87	9.89
	Impulse	6.64	66.14	28.70	7.39	45.72	29.05	7.33	23.58	14.47	4.08	31.31	18.13	2.92	53.45	20.41	6.51	29.65	18.32	2.37	15.70	7.48	3.57	35.67	14.45
	Speckle	3.90	62.01	20.64	4.22	34.96	17.18	5.47	25.52	15.60	5.32	25.22	12.66	1.95	46.32	12.89	6.62	26.05	16.48	1.32	12.57	4.19	2.74	26.83	8.00
	Shot	3.52	56.71	17.77	4.36	31.67	17.77	5.75	26.02	16.01	3.15	23.11	11.59	1.86	40.44	11.98	6.74	25.64	17.08	1.16	9.87	3.92	2.59	23.75	7.88
Quality	Pixelate	1.96	68.09	18.71	1.60	45.83	6.78	1.48	31.68	2.59	1.11	25.86	1.78	1.22	50.63	2.90	1.65	21.47	2.00	0.77	7.74	0.88	0.92	8.67	2.22
	JPEG	3.32	83.54	27.92	2.09	41.69	12.82	2.89	42.62	14.96	1.92	38.70	11.51	2.95	53.97	18.08	3.19	37.72	13.67	2.56	31.00	11.85	2.88	49.15	15.91
	Elastic	1.37	40.00	6.89	1.16	32.49	5.54	2.62	35.78	11.01	1.24	27.24	6.40	1.08	34.62	4.77	1.33	19.43	4.78	0.79	16.27	2.12	1.42	28.18	5.47
Weather	Fog	0.80	14.42	5.32	0.91	10.32	6.33	0.86	9.66	5.67	0.84	11.21	6.42	5.20	28.15	19.97	1.97	12.01	7.11	1.74	11.77	7.82	16.84	20.96	12.89
	Frost	8.20	63.96	29.96	7.38	29.96	21.25	8.18	34.19	23.87	8.13	34.30	22.31	6.97	45.13	30.13	8.37	32.75	21.76	7.22	33.69	21.15	8.27	50.31	27.44
	Rain	8.60	64.20	32.72	19.99	36.74	31.22	11.13	33.50	20.83	33.00	43.98	36.18	18.20	68.87	56.38	42.41	38.89	31.99	63.71	48.25	41.15	40.18	73.51	57.05
	Snow	3.60	70.60	29.90	4.69	33.21	30.91	7.92	40.20	33.82	5.30	40.82	33.35	12.08	74.27	66.65	7.16	37.04	31.37	39.79	68.67	61.60	39.73	90.80	81.91
	Spatter	6.58	67.90	27.09	6.63	28.22	20.24	8.41	40.38	26.92	7.75	36.11	21.81	5.71	48.60	33.82	7.98	30.37	19.87	9.13	45.03	28.99	9.33	65.41	40.19
Average		2.98	40.89	14.68	3.62	23.39	12.21	3.77	21.53	11.21	4.03	21.47	10.95	4.29	38.32	19.18	5.64	20.18	11.47	7.01	18.84	11.09	7.25	31.71	16.44
Median		1.92	48.35	13.83	1.71	29.09	6.95	2.14	24.55	8.89	1.39	23.93	6.79	2.82	41.33	13.88	2.60	22.13	7.36	1.47	12.17	4.90	2.77	26.85	7.94
Clean Error		0.94	10.36	2.95	0.64	5.72	2.19	0.72	6.51	2.38	0.91	7.07	3.08	4.16	29.96	12.87	1.48	6.79	3.20	1.04	6.71	2.82	2.29	82.27	4.89

Table 2. Initial RobustSpring results on corruption robustness of optical flow models, using R_{EPE}^c , R_{1px}^c and R_{FI}^c between clean and corrupted flow predictions. Low values indicate robust models. *Clean Error* compares clean predictions and ground-truth flows, values from [43].

Robustness Ranking. Because we generate 20 different corruption evaluations *per* dense matching model, we need a summarization strategy to produce one result per model. Per-model results are ranked based on three strategies: Average, Median, and the Schulze voting method [64]. In contrast to averaging across all 20 evaluations, the median reduces the impact of extreme outliers. The Schulze method provides a holistic, pairwise comparison approach that ranks models based on preference aggregation and was used for prior generalization evaluations in the Robust Vision Challenges. We evaluate their differences in Sec. 4.2

3.3. Dataset and Benchmark Functionality

Below, we summarize RobustSpring’s corruption dataset and describe its benchmark function. Dataset and benchmark will be at spring-benchmark.org. Fig. 3 shows data samples with stereo, optical flow and scene flow estimates.

RobustSpring Dataset. The final RobustSpring dataset entails 20 corrupted versions of Spring, resulting in 40,000 frames, or 20,000 stereo frame pairs. Each corruption evaluation yields 3960 optical flows (990 per camera & direction), 2000 stereo disparities (1000 per camera) and 3960 additional scene flow disparity maps (990 per camera per direction). We publicly release the RobustSpring test set licensed with CC BY 4.0, but no corrupt training data to discourage corruption finetuning for a fair benchmark.

RobustSpring Benchmark. RobustSpring enables uploading robustness results to a benchmark website for display in a public ranking. To emphasize that robustness and ac-

curacy are two axes of model performance with equal importance [71], we couple RobustSpring with Spring’s established accuracy benchmark. Thus, researchers can report model robustness and accuracy on the same dataset. To maintain Spring’s upload policy, 3 per 30 days, one per hour, each submission receives one robustness upload.

4. Results

We evaluate RobustSpring under two aspects: First, we report initial results for 16 optical flow, scene flow and stereo models. Then, we analyze the benchmark evaluation, particularly subsampling strategy and ranking methods.

4.1. Initial RobustSpring Benchmark Results

We provide initial results on RobustSpring for selected models from all three dense matching tasks. For optical flow, we include GMFlow [76], MS-RAFT+ [26, 27], FlowFormer [23], GMA [28], SPyNet [52], RAFT [69], FlowNet2 [24], and PWCNet [65]. For scene flow, we evaluate M-FUSE [42] and RAFT-3D [70]. For stereo estimation, we evaluate RAFT-Stereo [36], ACVNet [75], LEAStereo [13], and GANet [79]. An overview of all models and used checkpoints is in Tab. A1. Importantly, none of these models are fine-tuned to either Spring or RobustSpring data, to assess the generalization capacity of existing models.

Optical Flow. The evaluation results in Tab. 2 show considerable robustness variations over the different corruption types, which we also visualize in Fig. 4a. Weather-based corruptions, especially rain and snow, degrade the perfor-

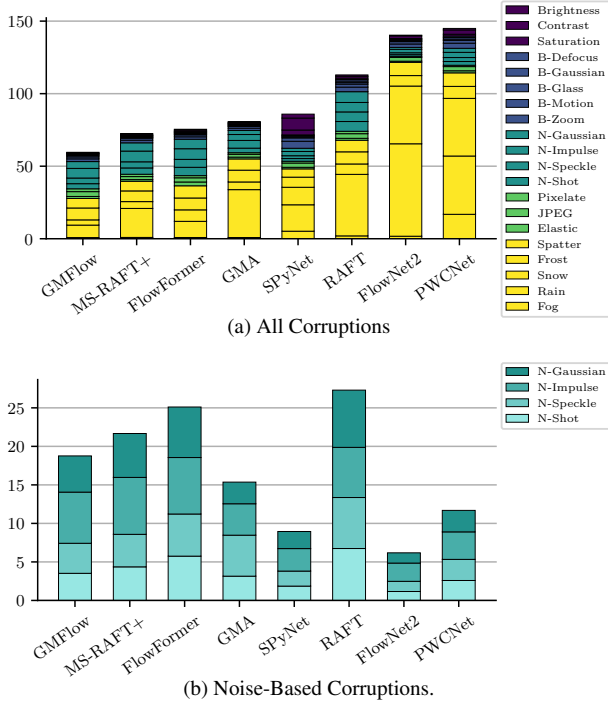


Figure 4. Accumulated corruption robustness R_{EPE}^c for optical flow models over all corruptions [top] and only noise corruptions [bottom]. All other corruption classes color (purple), blur (blue), noise (cyan), quality (green), and weather (yellow) are in Fig. A3.

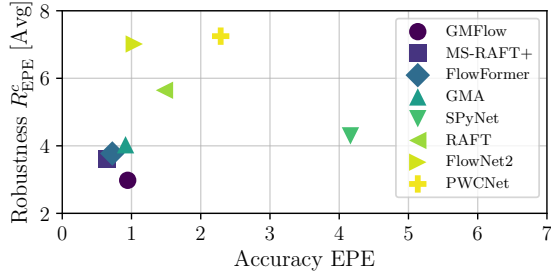


Figure 5. Accuracy vs. robustness of optical flow models, measured as EPE and Averaged R_{EPE}^c . Small values indicate accurate and robust models. Fig. A2 shows accuracy vs. Median R_{EPE}^c .

mance most and lead to the largest R^c values. In contrast, color-based corruptions have a relatively small impact, as most models maintain low R_{EPE}^c values. Also, the order of models can change significantly depending on the corruption type. While FlowNet2 does not perform well in the overall comparison, it is the best model for noise-based corruptions in Figure 4b. Overall, GMFlow achieves the lowest average R_{EPE}^c , GMA the lowest median. We will detail on ranking differences in Sec. 4.2.

To investigate a potential accuracy-robustness tradeoff on image corruptions, we visualize both quantities in 5. Overall, accurate models tend to be more robust, though we find a slight tradeoff because there is no unanimous win-

		M-FUSE						RAFT-3D					
		Optical flow			Disparity 2			Optical flow			Disparity 2		
		R_{EPE}^c	R_{1px}^c	R_{FI}^c	R_{Abs}^c	R_{1px}^c	R_{D2}^c	R_{EPE}^c	R_{1px}^c	R_{FI}^c	R_{Abs}^c	R_{1px}^c	R_{D2}^c
Color	Brightness	0.83	5.54	2.80	0.14	1.53	0.18	1.38	8.23	3.87	0.07	1.48	0.21
	Contrast	0.99	7.86	3.60	0.17	1.71	0.17	1.42	10.71	5.07	0.07	1.65	0.22
	Saturate	0.67	4.94	2.43	0.12	1.22	0.14	0.93	6.72	3.31	0.06	1.33	0.18
Blur	Defocus	0.84	5.26	2.71	0.15	1.37	0.15	0.66	5.27	2.44	0.04	0.88	0.10
	Gaussian	0.94	5.81	2.92	0.16	1.56	0.18	0.78	5.85	2.73	0.05	1.04	0.14
	Glass	0.80	5.17	2.65	0.16	1.32	0.14	0.65	5.29	2.39	0.04	0.82	0.09
	Motion	1.51	15.10	6.81	0.18	2.50	0.35	1.62	14.66	6.85	0.08	1.60	0.28
	Zoom	2.28	27.88	9.52	0.28	3.74	0.41	2.68	34.06	11.99	0.14	2.84	0.50
	Gaussian	6.49	29.22	14.81	0.41	6.56	0.80	5.25	43.33	25.43	0.20	3.64	0.71
Noise	Impulse	5.98	37.32	19.16	0.43	8.11	0.88	6.73	59.86	33.16	0.22	4.43	0.75
	Speckle	3.73	29.39	12.22	0.35	5.68	0.57	4.86	51.12	26.11	0.18	3.17	0.64
	Shot	4.87	26.32	12.34	0.36	5.60	0.69	4.65	42.07	22.91	0.18	3.26	0.67
Quality	Pixelate	0.86	5.95	2.51	0.19	1.51	0.13	0.82	7.66	2.83	0.05	1.02	0.10
	JPEG	1.98	27.21	6.82	0.32	3.62	0.36	2.73	33.93	10.55	0.13	2.59	0.41
	Elastic	1.15	14.93	3.92	0.22	2.28	0.22	1.70	21.82	5.99	0.08	1.61	0.20
	Fog	2.35	15.39	10.13	0.19	2.43	0.19	2.29	18.15	11.67	0.06	1.23	0.15
Weather	Frost	7.91	41.60	23.41	0.38	6.55	0.78	7.49	45.07	24.26	0.16	3.75	0.52
	Rain	10.21	41.78	28.99	0.70	12.79	1.29	27.89	74.23	59.77	0.47	10.75	1.96
	Snow	6.36	47.06	33.55	0.46	7.67	0.80	19.08	80.49	60.01	0.31	6.79	0.84
	Spatier	7.00	46.35	22.10	0.39	6.21	0.80	7.06	55.55	25.80	0.17	3.82	0.53
Average		3.39	22.00	11.17	0.29	4.20	0.46	5.03	31.20	17.36	0.14	2.89	0.46
Median		2.13	20.86	8.17	0.25	3.06	0.35	2.49	27.88	11.11	0.10	2.12	0.35
Clean Error		2.52	13.96	6.89	7.11	32.95	14.54	2.53	20.98	8.48	8.08	57.03	21.54

Table 3. Initial RobustSpring results on corruption robustness of scene flow models. Corresponding Disparity 1 from LEAStereo (s) for M-FUSE, and GANet (s) for RAFT-3D in Tab. 4.

ner in both dimensions – similarly for median robustness in Fig. A2. Interestingly, this contrasts with adversarial robustness evaluations, which observed a clear accuracy-robustness tradeoff on optical flow [60]. Potentially, this tradeoff is less pronounced for image corruptions as they are not optimized per model like adversarial attacks.

Focusing on the architecture of optical flow models, we find that transformer-based models, such as GMFlow and FlowFormer, generally outperform other architectures. However, they tend to struggle with noise corruptions, potentially resulting from their global matching. Hierarchical models, such as MS-RAFT+, achieve balanced performance for most corruptions and may benefit from multi-scale feature processing to cope with quality degradations. In contrast, stacked architectures such as FlowNet2 are uniquely resilient to noise, potentially due to their progressive refinement across layers. Overall, certain architectural features appear to influence robustness to certain corruption types, but there is no clear winner in terms of architecture.

Scene Flow. The results for scene flow are in Tab. 3, and include optical flow and target frame disparity predictions for M-FUSE and RAFT-3D. M-FUSE generally produces more robust optical flow across corruptions with a lower average R_{EPE}^c than RAFT-3D. But both methods suffer significant performance losses for severe weather like rain and noise-based corruptions, e.g. impulse noise. Interestingly, their robustness does not improve compared to conventional optical flow models. Noise and weather corruptions remain a challenge for Disparity 2 predictions. Here, RAFT-3D consistently achieves lower robustness scores compared to M-FUSE, but conditions like impulse noise or rain still notably

		RAFT-Stereo (s)			ACVNet (s)			LEAStereo (s)			LEAStereo (k)			GANet (k)			GANet (s)		
		R_{1px}^c	R_{Abs}^c	R_{D1}^c	R_{1px}^c	R_{Abs}^c	R_{D1}^c	R_{1px}^c	R_{Abs}^c	R_{D1}^c	R_{1px}^c	R_{Abs}^c	R_{D1}^c	R_{1px}^c	R_{Abs}^c	R_{D1}^c	R_{1px}^c	R_{Abs}^c	R_{D1}^c
Color	Brightness	8.98	2.13	2.83	19.82	6.89	8.80	6.38	1.27	1.78	11.57	2.02	3.73	12.46	2.48	4.61	10.74	2.11	3.39
	Contrast	14.04	2.62	3.81	19.33	8.34	9.88	19.00	3.33	6.45	18.23	2.86	5.63	18.02	2.72	5.49	23.14	3.94	6.74
	Saturate	7.54	0.74	0.95	8.12	3.18	3.79	6.43	1.24	1.71	13.57	3.05	4.64	16.69	3.53	5.77	13.53	2.70	3.86
Blur	Defocus	10.61	2.47	3.90	8.06	1.10	1.90	8.55	2.02	2.49	29.31	3.26	5.21	41.32	3.29	4.68	12.34	2.46	3.16
	Gaussian	11.40	2.57	3.97	9.29	1.55	2.38	9.64	2.16	2.65	48.95	3.68	5.54	47.97	3.55	4.98	13.76	2.69	3.45
	Glass	13.10	2.61	3.34	11.72	1.31	1.95	11.56	2.17	2.55	70.01	4.79	6.36	71.45	4.33	5.18	19.42	2.61	3.15
	Motion	12.41	2.30	2.61	9.72	1.13	2.07	10.59	1.82	2.74	20.04	2.44	4.77	16.99	2.27	4.26	13.12	2.31	3.61
Noise	Zoom	59.50	5.86	7.19	64.76	6.43	9.32	63.52	6.38	9.74	74.92	8.84	16.83	74.29	8.18	14.80	59.89	7.29	11.21
	Gaussian	40.76	20.44	24.16	56.40	39.19	37.76	80.74	80.89	62.28	65.13	15.23	24.53	49.20	7.90	13.17	85.78	33.35	45.02
	Impulse	44.79	21.16	27.99	69.34	53.14	49.67	85.39	85.24	65.42	69.03	17.24	25.47	51.64	8.18	12.70	85.00	38.94	50.45
	Speckle	42.58	13.64	21.85	71.99	63.51	57.36	84.06	84.54	65.37	66.23	15.68	24.31	55.36	7.64	13.63	83.70	29.65	41.90
Quality	Shot	39.84	15.55	20.23	59.56	42.20	41.10	79.41	76.53	59.94	64.06	14.29	22.95	49.36	6.95	11.98	81.49	28.20	39.89
	Pixelate	66.69	46.19	13.86	57.29	4.14	4.98	35.19	3.85	4.11	57.19	3.72	4.83	62.71	4.00	4.60	59.61	3.70	4.07
	JPEG	55.27	8.24	5.27	60.87	15.98	15.16	55.18	9.20	10.84	68.22	5.63	7.97	65.92	7.41	11.19	59.52	6.76	10.10
Weather	Elastic	65.53	6.52	4.32	58.39	8.17	7.29	71.96	8.02	10.92	93.40	7.16	8.90	87.38	6.89	8.86	76.47	4.85	5.05
	Fog	13.71	1.57	2.10	17.99	17.70	12.12	17.95	14.25	10.88	23.36	8.18	12.90	21.36	9.69	12.45	20.55	9.68	9.75
	Frost	41.63	18.84	10.68	39.79	8.15	19.27	38.43	7.28	18.51	53.98	12.37	23.89	39.74	9.84	20.93	47.40	11.20	24.31
	Rain	43.10	79.42	32.27	34.62	12.92	18.48	56.55	22.14	34.58	65.45	12.54	28.62	49.08	11.44	22.55	59.22	26.50	42.34
	Snow	41.05	51.30	32.90	40.96	18.62	29.03	47.03	20.51	32.23	52.16	13.88	29.40	35.16	11.83	22.94	45.88	17.24	33.30
Average	Spatier	35.50	27.17	12.57	18.01	2.18	3.85	31.43	5.13	10.19	35.54	7.93	14.24	28.00	6.75	12.42	34.58	6.04	13.86
	Average	33.40	16.57	11.84	36.80	15.79	16.81	40.95	21.90	20.77	50.02	8.24	14.04	44.71	6.44	10.86	45.26	12.11	17.93
Median		40.30	7.38	6.23	37.21	8.16	9.60	36.81	6.83	10.51	55.58	7.55	10.90	48.53	6.92	11.58	46.64	6.40	9.93
Clean		15.27	3.02	5.35	14.77	1.52	5.35	19.89	3.88	9.19	47.50	6.15	17.16	27.91	5.29	11.56	23.22	4.59	10.39

Table 4. Initial RobustSpring results on corruption robustness of stereo disparity models, using corruption robustness R_{1px}^c , R_{Abs}^c and R_{D1}^c between clean and corrupted predictions. Low values indicate robust models, using Stereo (s) and KITTI (k) checkpoints, *cf.* Tab. A1.

affect disparity predictions. Overall, both models have limited robustness, but temporal consistency may contribute to lower robustness scores under several corruption types.

Stereo. The results of the stereo disparity estimations are presented in Tab. 4. The effect of the different corruptions on the performance is significant, with noise and weather-based corruptions leading to the largest errors, especially for GANet and LEAStereo. In particular, Gaussian and impulse noise introduce extremely large errors, highlighting the sensitivity of stereo models to pixel-level noise. Blur distortions, especially zoom blur, also have a severe impact on all models, with high 1px and D1 errors. In contrast, color-based distortions generally yield smaller errors. RAFT-Stereo shows stronger resilience across most corruption groups, performing better on color and noise based corruption than other models. However, it also struggles with noise and severe weather effects such as rain and snow.

4.2. Metrics and Benchmark Capability

After reporting initial RobustSpring results, we analyze aspects of its benchmark character: The subsampling strategy for data efficiency, and different ranking systems for result comparisons across 20 different prompt variations. We also validate our robustness metric for object corruptions and explore RobustSpring’s transferability to the real-world.

Subsampling. We evaluate RobustSpring’s strict data subsampling by comparing to results on the full test set. As shown in Tab. 5, our subsampling strategy produces results

	Subsampling R_{EPE}^c				Subsampling R_{1px}^c			
	Full	Spring	Spring*	Ours	Full	Spring	Spring*	Ours
% Original Data	100%	1.00%	0.94%	0.05%	100%	1.00%	0.94%	0.05%
GMFlow	2.98	3.20	2.98	2.98	40.89	41.99	40.89	40.89
MS-RAFT+	3.62	3.84	3.62	3.62	23.38	24.44	23.39	23.39
FlowFormer	3.77	3.89	3.77	3.77	21.52	22.39	21.53	21.53
GMA	4.03	4.28	4.03	4.03	21.47	22.59	21.48	21.47
SPyNet	4.30	4.56	4.29	4.29	38.32	39.28	38.32	38.32
RAFT	5.64	6.15	5.64	5.64	20.17	21.20	20.18	20.18
FlowNet2	7.01	7.36	7.01	7.01	18.84	19.79	18.84	18.84
PWCNet	7.25	7.52	7.25	7.25	31.71	32.55	31.72	31.71

Table 5. Influence of subsampling. We compare robustness evaluations on the full test data (Full) to evaluations on Spring’s original subsampling (Spring), original subsampling without Hero-frames (Spring*), and our refined corruption subsampling (Ours).

that are nearly identical to those that include all pixels in the robustness calculation. We observe the largest discrepancy for Spring’s original subsampling, because it includes a handful of full-resolution Hero-frames. If those frames are also subsampled (Spring*), results align with the full dataset. Overall, our stricter subsampling to 0.05% of all data is not only data efficient but also exact.

Metric Ranking. To explore how ranking strategies influence the optical-flow robustness order, we contrast our three summarization strategies: Average, Median, and Schulze, *cf.* Appendix C.3. The rankings in Tab. 6 notably differ across strategies. The Average differs most from the other rankings. For example, it ranks GMFlow 1st, which is only 4th on Median and Schulze, suggesting a good performance across corruptions without excessive outliers but no

Rank	Ranking Method		
	Average R_{EPE}^c	Median R_{EPE}^c	Schulze
1	2.98 GMFlow	1.39 GMA	MS-RAFT+
2	3.62 MS-RAFT+	1.47 FlowNet2	GMA
3	3.77 FlowFormer	1.71 MS-RAFT+	FlowNet2
4	4.03 GMA	1.92 GMFlow	GMFlow
5	4.29 SPyNet	2.14 FlowFormer	FlowFormer
6	5.64 RAFT	2.60 RAFT	SPyNet
7	7.01 FlowNet2	2.77 PWCNet	PWCNet
8	7.25 PWCNet	2.82 SPyNet	RAFT

Table 6. Robustness ranking of optical flow models with ranking strategies Average R_{EPE}^c , Median R_{EPE}^c , and Schulze to summarize results over corruptions. Schulze does not produce numeric values.

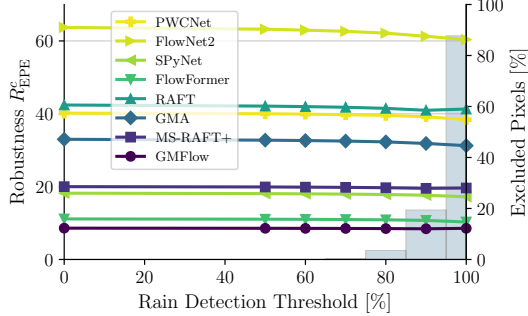


Figure 6. Stability of corruption robustness R_{EPE}^c on rain corruption. Robustness scores and method rankings remain stable even if we exclude all rain pixels (90% of all pixels) from R_{EPE}^c calculation, which places dominating prediction errors in the background *beyond* the moving particles. Results for snow are in Fig. A4.

top performance on most corruptions. Interestingly, Median and Schulze rankings are more aligned. As Schulze’s ranking involves complex comparisons of per-corruption rankings and must be globally recomputed for new models, the Median ranking is a cheap approximation to it. The ranking strategy has significant implications for selecting robust models. No model is optimal across rankings, and the rankings accentuate different aspects: overall performance, outlier robustness, or balanced performance in pairwise comparisons. Hence, RobustSpring reports them all.

Corruption Robustness on Object Corruptions. Intuitively, models are robust if they recover the main scene despite image corruptions. Here, we investigate if the corruption robustness metric faithfully represents model robustness even if corruptions like rain introduce moving objects to the scene. To this end, we contrast the robustness score contributions of background and corruption objects, by excluding pixels of objects like rain drops from the score calculation. We detect object pixels by taking the value difference d between original and corrupt images, and exclude them if $(1 - d)$ is above a detection threshold. Threshold 0 detects no rain pixels, matching the vanilla R_{EPE}^{Rain} , while 100 detects all. Figure 6 shows the robustness score if rain is excluded from the calculation, along with bars indicating the amount [%] of excluded pixels. Remarkably, the robustness score is stable, *i.e.* varies $\leq 5\%$, even for discarding *all* rain

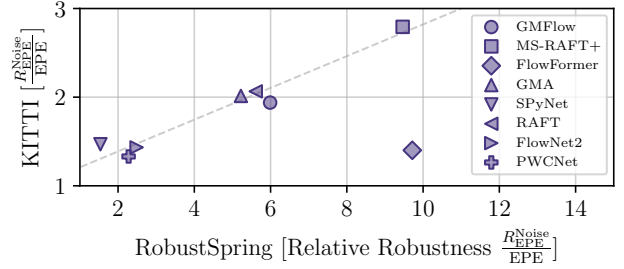


Figure 7. Relative robustness to noise on RobustSpring transfers to noisy real-world KITTI data [45] for most optical flow models.

pixels, *i.e.* 90% of all pixels. Large robustness scores on rain or snow, *cf.* Fig. A4, thus stem from mispredictions in the *periphery* of altered pixels, not from motion predictions on altered pixels. As it is dominated by scene-wide effects, our corruption robustness yields stable robustness rankings that make it suited for broad model robustness evaluations.

Robustness in the Real World. Finally, we investigate if RobustSpring’s corruption robustness transfers to the real world. To this end, we select the noisiest 10% KITTI data, estimating noise as in [25]. These noisy KITTI frames have no clean counterparts to calculate corruption robustness R_{EPE}^{Noise} . Thus, we approximate R_{EPE}^{Noise} via the accuracy difference on noisy and non-noisy KITTI frames. To account for model-specific performance differences on Spring and KITTI, we normalize with the clean dataset performance and show the resulting relative robustness $\frac{R_{EPE}^{\text{Noise}}}{R_{EPE}^{\text{Clean}}}$ in Fig. 7. Relatively robust models with low scores on RobustSpring are also robust on KITTI and vice versa. The only outlier, FlowFormer, overperforms on KITTI, potentially due to outstanding memorization capacity and exposure to KITTI during training. Because overall noise resilience on RobustSpring qualitatively transfers to KITTI, RobustSpring supports model selection for real-world settings where corruption robustness cannot be measured.

5. Conclusion

With RobustSpring we introduce an image corruption dataset and benchmark that evaluates the robustness of optical flow, scene flow and stereo models. We carefully design 20 different image corruptions and integrate them in time, stereo, and depth for a holistic evaluation of dense matching tasks. Furthermore, we establish a corruption robustness metric using clean and corrupted predictions, and compare ranking strategies to unify model results across all 20 corruptions. RobustSpring’s benchmark further supports data-efficient result uploads to a public website. Our initial evaluation of 16 optical flow, scene flow and stereo models reveals an overall high sensitivity to corrupted images. As our robustness results translate to real-world performance, systematic corruption benchmarks like RobustSpring are crucial to uncover potential model performance improvements.

Limitations. Due to its benchmark character, we have limited the image corruptions on RobustSpring to a selection of 20. While this does not cover the full space of potential corruptions, this data-budget limitation is necessary to make the RobustSpring dataset applicable and not overburden the computational resources of researchers during evaluation.

Acknowledgements. Jenny Schmalfuss and Andrés Bruhn acknowledge support by the Deutsche Forschungsgemeinschaft (DFG, German Research Foundation) – Project-ID 533085500. Furthermore, Jenny Schmalfuss and Victor Oei acknowledge funding by the DFG – Project-ID 251654672 – TRR 161 (B04). Margret Keuper would like to acknowledge support by the DFG Research Unit 5336 – Learning to Sense (L2S). The authors thank the International Max Planck Research School for Intelligent Systems (IMPRS-IS) for supporting Jenny Schmalfuss and Victor Oei.

RobustSpring: Benchmarking Robustness to Image Corruptions for Optical Flow, Scene Flow and Stereo

Supplementary Material

A. Repository Links and Checkpoints

To support reproducibility, Tab. A1 reports the repositories and checkpoints for the optical flow, scene flow and stereo models, which were benchmarked on RobustSpring in Tab. 2, Tab. 4 and Tab. 3. Further details on training and checkpoints for these models can be found in their original publications.

B. RobustSpring Image Corruptions

Below, we provide supplementary information on the image corruptions for the RobustSpring dataset. Besides visualizing further benchmark samples, we also give details on their implementation with a focus on RobustSpring-specific consistencies.

B.1. Additional Corruption Benchmark Samples

To complement the benchmark samples in Fig. 3, we show benchmark results on additional corruptions in Fig. A1.

B.2. Corruption Implementation

Below we provide the implementation details and parameters for all corruptions in the RobustSpring dataset. We cluster the corruptions by their main classes. The original (uncorrupted) image is denoted as I , while the corrupted version is \hat{I} . The pixel-aligned depth values are D . In the stereo video setting, the image subscripts t and $t+1$ denote frames over time, while l and r denote left and right frame, where necessary. All of RobustSpring’s noises are independent of time, stereo and depth, which means they are sampled independently for every single image of the dataset.

Brightness. The brightness is adapted via

$$\hat{I} = I + c, \quad (4)$$

and for time- and stereo-consistent brightness changes in RobustSpring we choose the parameter $c = c_t^l = c_t^r = c_{t+1}^l = c_{t+1}^r = 0.39$.

Contrast. The equation to adapt contrast is

$$\hat{I} = (I - \text{mean}(I)) \cdot c + \text{mean}(I), \quad (5)$$

where we selected $c = c_t^l = c_t^r = c_{t+1}^l = c_{t+1}^r = 0.16$ for time- and stereo-consistent contrast adaptations.

Saturation. For those adaptations the RGB image is transformed to HSV, and the saturation component S is adapted via

$$\hat{S} = S \cdot \alpha + \beta, \quad (6)$$

with $\alpha = \alpha_t^l = \alpha_t^r = \alpha_{t+1}^l = \alpha_{t+1}^r = 2.3$ and $\beta_t^l = \beta_t^r = \beta_{t+1}^l = \beta_{t+1}^r = 0.01$ for time- and stereo-consistent saturation changes.

Defocus Blur. The defocus blur convolves the image with a circular mean filter C_r^{mean}

$$\hat{I} = I * C_r^{\text{mean}}, \quad (7)$$

where we choose the radius $r = r_t^l = r_t^r = r_{t+1}^l = r_{t+1}^r = 6$ for time- and stereo-consistent blurring.

Gaussian Blur. Gaussian blur convolves the image with a Gaussian C_σ^{Gauss}

$$\hat{I} = I * C_\sigma^{\text{Gauss}}, \quad (8)$$

where we choose the standard deviation $\sigma = \sigma_t^l = \sigma_t^r = \sigma_{t+1}^l = \sigma_{t+1}^r = 4$ for time- and stereo-consistent blurring.

Glass Blur. This is a Gauss-blurred image, whose pixels are afterwards shuffled via the shuffling $S(I, i, r)$ over several iterations i within a neighborhood of radius r

$$\hat{I} = S(I * C_\sigma^{\text{Gauss}}, i, r), \quad (9)$$

where two sets of time-consistent parameters are picked for the different stereo cameras: $\sigma_t^l = \sigma_{t+1}^l = 1.2$, $\sigma_t^r = \sigma_{t+1}^r = 1.2$, $i_t^l = i_{t+1}^l = 1$, $i_t^r = i_{t+1}^r = 1$, $r_t^l = r_{t+1}^l = 3$ and $r_t^r = r_{t+1}^r = 3$.

Motion Blur. Motion blur is implemented by averaging the intensities of pixels along the motion trajectory determined by the optical flow. Let $\mathbf{v}(x, y) = (v_x(x, y), v_y(x, y))$ be the optical flow vector at pixel (x, y) , and let

$$N = \max \left(1, \left\lfloor 10 \cdot \max_{(x, y)} \|\mathbf{v}(x, y)\| \right\rfloor \right) \quad (10)$$

be the number of samples along the motion path. Then, the blurred pixel is computed as

$$\hat{I}(x, y) = \frac{1}{N+1} \sum_{k=0}^N I \left(x + \frac{k}{N} v_x(x, y), y + \frac{k}{N} v_y(x, y) \right). \quad (11)$$

Here, the scaling factor 10 controls the extent of the blur relative to the magnitude of the motion.

Zoom Blur. Zoom blur is created by averaging the original image with a series of zoomed-in versions of itself. Specifically, let $Z(I, z)$ denote the image I zoomed by a factor z , and let $\{z_i\}$ be a set of zoom factors ranging from 1 to

Method	Repository	Checkpoint
Optical Flow		
RAFT	https://github.com/princeton-vl/RAFT	Sintel
PWCNet	https://github.com/NVlabs/PWC-Net	Sintel
GMFlow	https://github.com/haofeixu/gmflow	Sintel
GMA	https://github.com/zacjiang/GMA	Sintel
FlowNet2	https://github.com/NVIDIA/flownet2-pytorch	Sintel
FlowFormer	https://github.com/drinkingcoder/FlowFormer-Official	Sintel
MS-RAFT+	https://github.com/cv-stuttgart/MS-RAFT_plus	Mixed*
SPyNet	https://github.com/anuragranj/flowattack (PyTorch implementation) https://github.com/anuragranj/spynet (original implementation)	Sintel
Scene Flow		
M-FUSE	https://github.com/cv-stuttgart/M-FUSE	KITTI 2015
Stereo		
RAFT-Stereo	https://github.com/princeton-vl/RAFT-Stereo/	Scene Flow (s)
ACVNet	https://github.com/gangweiX/ACVNet	Scene Flow (s)
LEAStereo	https://github.com/XuelianCheng/LEAStereo	Scene Flow (s), KITTI (k)
GANet	https://github.com/feihuzhang/GANet	Scene Flow (s), KITTI (k)

Table A1. Repositories and checkpoints used for evaluating methods in RobustSpring. *The Mixed checkpoint MS-RAFT+ is pretrained on Chairs and Things and then fine-tuned on a mix of Sintel, Viper, KITTI 2015, Things, and HD1k.

approximately 1.24 (in increments of 0.02). Then the final image is computed as

$$\hat{I} = \frac{1}{N+1} \left(I + \sum_{i=1}^N Z(I, z_i) \right), \quad (12)$$

where N is the number of zoom factors. This formulation averages the original image with its progressively zoomed versions, resulting in a smooth zoom blur effect.

Gaussian Noise. This noise adds a random value from a Normal distribution to every pixel in the original image, where $\mathcal{N}_I(\mu, \sigma^2)$ is a I -shaped array of random numbers that are drawn from the Normal distribution with mean μ and variance σ^2 :

$$\hat{I} = I + \alpha \cdot \mathcal{N}_I(0, 1). \quad (13)$$

The scaling $\alpha = 0.115$ is selected for all images in RobustSpring, but $\mathcal{N}_I(0, 1)$ is sampled anew for every image.

Impulse Noise. Here, for a fixed fraction of pixels p , their values are replaced by the values 0 or 255. For RobustSpring, $p = 0.075$.

Speckle Noise. Like Gaussian noise, Speckle noise also builds on random values from a Normal distribution, but adds these values after additionally scaling with I :

$$\hat{I} = I + I \cdot \alpha \cdot \mathcal{N}_I(0, 1). \quad (14)$$

For RobustSpring, the parameter is $\alpha = 0.45$.

Shot Noise. Shot noise uses values drawn from a Poisson distribution \mathcal{P} per pixel

$$\hat{I} = \frac{\mathcal{P}(I \cdot c)}{c}, \quad (15)$$

where $c = 23$ for RobustSpring.

Pixelation. This is achieved by downsampling the image to size s , a fraction of its original size, with a box filter $\text{box}(I, s)$, followed by upsampling $\text{up}(I, s)$ to the size s , which is the original size:

$$\hat{I} = \text{up}(\text{box}(I, I \cdot c), I). \quad (16)$$

For RobustSpring, we use the size fraction $c = c_t^l = c_t^r = c_{t+1}^l = c_{t+1}^r = 0.16$ for time- and stereo-consistent pixelation.

JPEG Compression. For JPEG compression, the quality q is the only variable parameter

$$\hat{I} = \text{JPEG}(I, q), \quad (17)$$

which is selected as $q = q_t^l = q_t^r = q_{t+1}^l = q_{t+1}^r = 6$ for time- and stereo-consistent JPEG compression.

Elastic Transformation. The elastic transformation applies an elastic deformation using `torchvision.transforms.v2` with parameters $\alpha = 110.0$ and $\sigma = 5.0$ to control the deformation magnitude and smoothness, while preserving the original frame dimensions.

Spatter. The spatter corruption simulates liquid droplets by generating a liquid layer from Gaussian noise, applying blur and thresholding, and blending it with the original image using a predefined color.

Frost. The frost corruption overlays a frost texture onto the image by randomly selecting and resizing a pre-stored

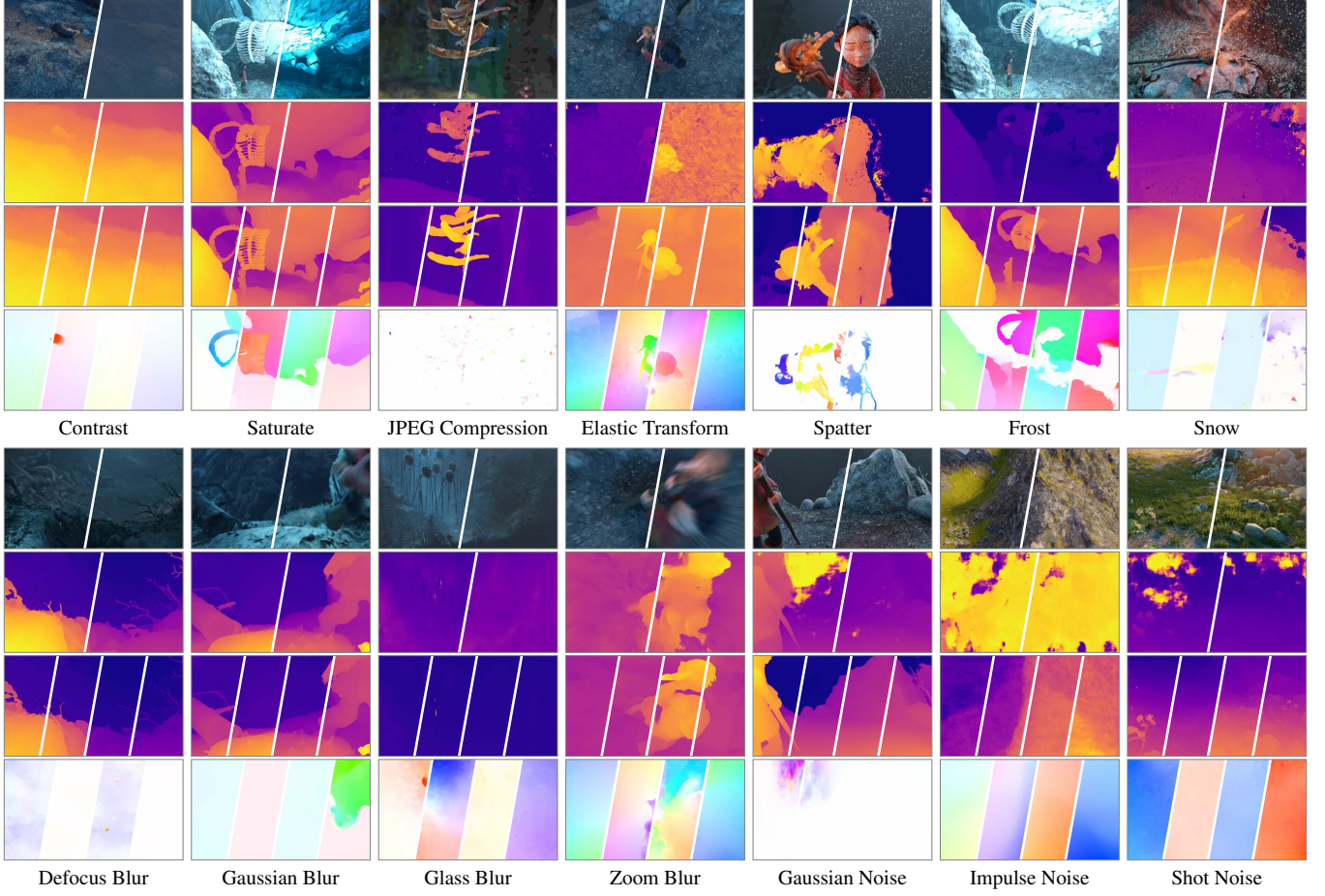


Figure A1. RobustSpring example frames, complementing Fig. 3. The first row shows clean and corrupted images. The second row shows the left and right disparity maps predicted with LEA Stereo [13]. The third row shows the target disparities for forward left, backward left, forward right, and backward right directions from M-FUSE [42]. The fourth row shows optical flow estimates for forward left, backward left, forward right, and backward right from RAFT [69]. All disparities and flows are computed on the corrupted dataset.

frost image and blending it with the input to create an icy appearance.

Snow and Rain. The implementation for snow and rain is based on [61], with methodological and performance improvements. On the methodological side, we replaced additive blending with order-independent alpha blending (Meshkin’s Method) [41] and included global illumination [19] in the color rendering. Also, we expanded the monocular two-step motion simulation to multi-step stereo images. On the performance side, we introduce an efficient parallel particle initialization and improve the parallel processing performance.

Fog. Fog is modelled using the Koschmieder model from [73] as

$$\hat{I} = I \cdot e^{-\frac{D \cdot \ln(20)}{d_m}} + l \cdot (1 - e^{-\frac{D \cdot \ln(20)}{d_m}}), \quad (18)$$

where d_m is the visibility range and l the luminance of the

sky. For RobustSpring, we use $d_m = 45$ and $l = 0.8$. As it directly depends on the depth D , this is depth-consistent and due to its integration into the 3D scene it is also stereo- and time-consistent.

C. Additional Experimental Results

Below, we expand on the experiments in the main paper and provide supplementary results for our major experiments.

C.1. Corruption Robustness by Corruption Group

Figure A3 shows the corruption robustness R_{EPE}^c for each optical flow method across the remaining four corruption groups in addition to Fig. 4 in the main paper. It underlines the varying degrees of robustness of the evaluated methods against specific types of corruption.

C.2. Accuracy vs. Median Corruption Robustness

In Fig. A2 we show the accuracy-robustness evaluation with the *Median* corruption robustness, to complement Fig. 5 which uses the average corruption robustness. Even though the robustness ranking of methods varies between average and media corruption robustness, *cf.* Sec. 4.2 for a discussion on ranking differences, the general trend that corruption robustness and accuracy are weakly correlated remains. However, there is still no clear winner, and an accuracy-robustness tradeoff persists among particularly accurate or robust methods.

C.3. Schulze Pairwise Comparison Matrix

The Schulze method is a ranking algorithm used to determine the most preferred candidate based on pairwise comparisons. We include a pairwise comparison matrix in Table A2 for our ranking. The table shows how often the method in row i is better than the method in column j , based on the number of corruptions where method i achieves a lower error than method j . The ranking process consists of the following steps:

1) Constructing the Pairwise Comparison Matrix. For each pair of methods, we count how many times one method achieves a lower EPE than the other across different corruptions. If method A has a lower EPE than method B in a given corruption, the corresponding entry in the matrix is incremented.

2) Computing the Strongest Paths. We define the strength of a path from method A to method B as the number of cases where A outperforms B . The strongest paths between methods are determined by considering indirect paths: if method A is better than method B , and method B is better than method C , then the strength of the indirect path from A to C is considered.

3) Determining the Final Ranking. Method A is ranked higher than method B if the strongest path from A to B is

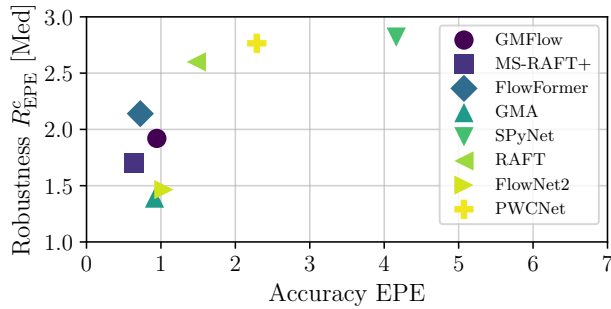
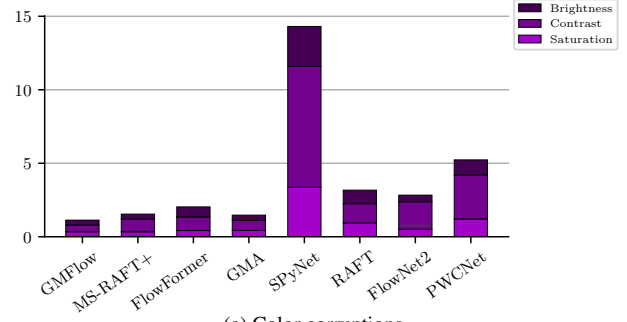
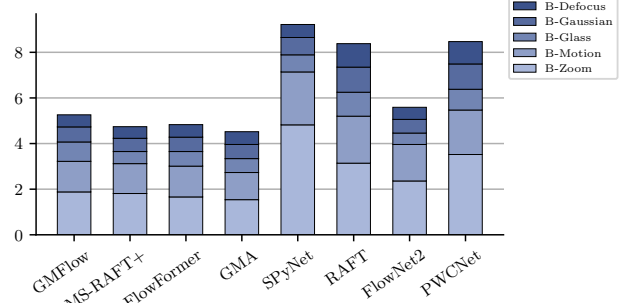


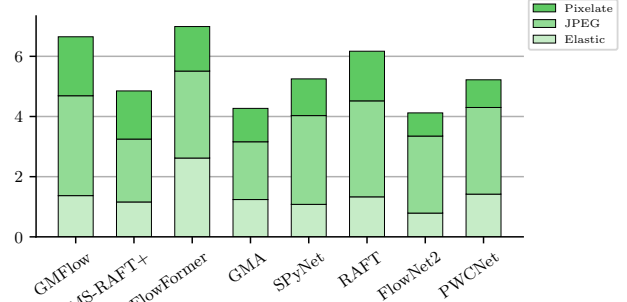
Figure A2. Accuracy vs. robustness of optical flow methods, measured as EPE and median R_{EPE}^c . Small values indicate accurate and robust methods. Fig. 5 shows the average R_{EPE}^c .



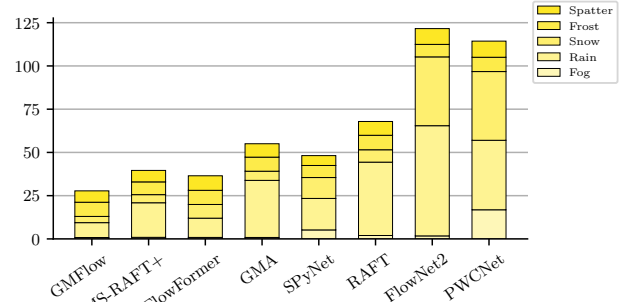
(a) Color corruptions.



(b) Blur corruptions.



(c) Quality corruptions.



(d) Weather corruptions.

Figure A3. Additional results on accumulated corruption robustness R_{EPE}^c for optical flow models over corruption classes color, blur, quality, and weather. More results are in Fig. 4.

stronger than the strongest path from B to A . This ensures that even if a method loses to another in some comparisons, it can still be ranked higher if it consistently performs well against other methods.

	GMFlow	GMA	MS-RAFT+	FlowFormer	SPyNet	RAFT	PWCNet	FlowNet2
GMFlow	0	9	7	16	10	16	14	12
GMA	11	0	9	19	12	17	14	14
MS-RAFT+	13	11	0	19	12	18	15	14
FlowFormer	4	1	1	0	8	9	13	8
SPyNet	10	8	8	12	0	12	14	5
RAFT	4	3	2	11	8	0	14	8
PWCNet	6	6	5	7	6	6	0	4
FlowNet2	8	6	6	12	15	12	16	0

Table A2. Pairwise comparison matrix for the Schulze method.

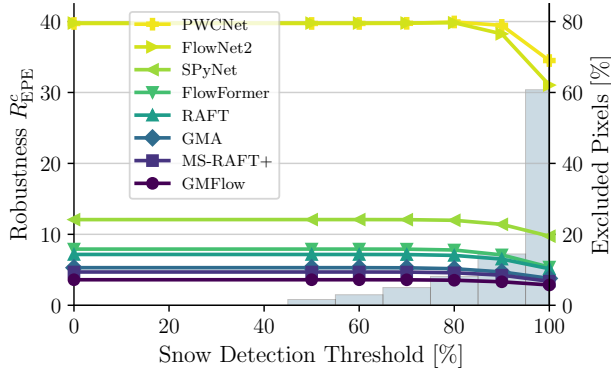


Figure A4. Stability of corruption robustness R_{EPE}^c for snow corruption. Analogous rain results in Fig. 6.

C.4. Corruption Robustness on Snow

Finally, we complement the evaluation of our corruption robustness metric in the presence of rain in Fig. 6 with the corresponding evaluation in the presence of snow in Fig. A4. The results with rain translate to snow with the following minor differences: Because snow has less motion blur than rain, it covers fewer pixels (60% of all pixels vs. 90% for rain). For snow, the score drops a bit more than for rain when object pixels are excluded ($\leq 25\%$ drop vs. $\leq 5\%$ for rain), potentially as a consequence of the increased object opacity for snow particles. Still, the background error ($\geq 75\%$ contribution to corruption robustness) dominates the score, and the robustness ranking for optical flow methods remains stable, whether snow pixels are included in the score calculation or not. Hence, the additional evaluation on snow further substantiates the stability and expressiveness of corruption robustness as an evaluation metric.

References

- [1] Shashank Agnihotri, Kanchana Vaishnavi Gandikota, Julia Grabinski, Paramanand Chandramouli, and Margret Keuper. On the unreasonable vulnerability of transformers for image restoration-and an easy fix. In *Proc. IEEE/CVF International Conference on Computer Vision Workshops (ICCVW)*, 2023. 2
- [2] Shashank Agnihotri, Julia Grabinski, Janis Keuper, and Margret Keuper. Beware of Aliases—Signal Preservation is Crucial for Robust Image Restoration. *arXiv preprint arXiv:2304.14736*, 2024.
- [3] Shashank Agnihotri, Julia Grabinski, and Margret Keuper. Improving Feature Stability during Upsampling – Spectral Artifacts and the Importance of Spatial Context. In *Proc. European Conference on Computer Vision (ECCV)*, 2024. 2
- [4] Shashank Agnihotri, Steffen Jung, and Margret Keuper. CosPGD: an efficient white-box adversarial attack for pixel-wise prediction tasks. In *Proc. International Conference on Learning Representations (ICML)*, pages 416–451, 2024. 2, 4
- [5] Shashank Agnihotri, Amaan Ansari, Annika Dackermann, Fabian Rösch, and Margret Keuper. DispBench. In *CVPR Workshop On Synthetic Data for Computer Vision*, 2025. 1, 2
- [6] Shashank Agnihotri, Julian Yuya Caspary, Luca Schwarz, Xinyan Gao, Jenny Schmalfuss, Andres Bruhn, and Margret Keuper. FlowBench: A robustness benchmark for optical flow estimation, 2025. 2
- [7] Shashank Agnihotri, Julian Yuya Caspary, Luca Schwarz, Xinyan Gao, Jenny Schmalfuss, Andres Bruhn, and Margret Keuper. Flowbench: A robustness benchmark for optical flow estimation, 2025. 1, 2
- [8] Shashank Agnihotri, David Schader, Nico Sharei, Mehmet Ege Kaçar, and Margret Keuper. Are Synthetic Corruptions A Reliable Proxy For Real-World Corruptions? In *CVPR Workshop On Synthetic Data for Computer Vision*, 2025. 2
- [9] Adithya Prem Anand, H. Gokul, Harish Srinivasan, Pranav Vijay, and Vineeth Vijayaraghavan. Adversarial patch defense for optical flow networks in video action recognition. In *IEEE International Conference on Machine Learning and Applications (ICMLA)*, pages 1289–1296, 2020. 2
- [10] Simon Baker, Daniel Scharstein, J. P. Lewis, Stefan Roth, Michael J. Black, and Richard Szeliski. A database and evaluation methodology for optical flow. *International Journal of Computer Vision (IJCV)*, 92(1):1–31, 2011. 1
- [11] Zachary Berger, Parth Agrawal, Tyan Yu Liu, Stefano Soatto, and Alex Wong. Stereoscopic universal perturbations across different architectures and datasets. In *Proc. IEEE/CVF Conference on Computer Vision and Pattern Recognition (CVPR)*, pages 15180–15190, 2022. 2
- [12] Daniel J. Butler, Jonas Wulff, G. B. Stanley, and Michael J. Black. A naturalistic open source movie for optical flow evaluation. In *Proc. European Conference on Computer Vision (ECCV)*, pages 611–625, 2012. 1, 2
- [13] Xuelian Cheng, Yiran Zhong, Mehrtash Harandi, Yuchao Dai, Xiaojun Chang, Hongdong Li, Tom Drummond, and Zongyuan Ge. Hierarchical neural architecture search for deep stereo matching. *Proc. Conference on Neural Information Processing Systems (NeurIPS)*, 33:22158–22169, 2020. 4, 5, 3
- [14] Francesco Croce, Maksym Andriushchenko, Vikash Sehwag, Edoardo Debenedetti, Nicolas Flammarion, Mung Chiang, Prateek Mittal, and Matthias Hein. RobustBench:

- a standardized adversarial robustness benchmark. In *Adv. Neural Inform. Process. Syst.*, 2021. 2
- [15] Alexey Dosovitskiy, Philipp Fischer, Eddy Ilg, Caner Hazirbas, Vladimir Golkov, Patrick van der Smagt, Daniel Cremers, and Thomas Brox. FlowNet: Learning optical flow with convolutional networks. In *Proc. IEEE/CVF International Conference on Computer Vision (ICCV)*, 2015. 2
- [16] Nathan Drenkow and Mathias Unberath. RobustCLEVR: A benchmark and framework for evaluating robustness in object-centric learning. In *Proc. IEEE/CVF Winter Conference on Applications of Computer Vision (WACV)*, pages 4518–4527, 2024. 2
- [17] Adrien Gaidon, Qiao Wang, Yohann Cabon, and Eleonora Vig. Virtual worlds as proxy for multi-object tracking analysis. In *Proc. IEEE/CVF Conference on Computer Vision and Pattern Recognition (CVPR)*, pages 4340–4349, 2016. 2
- [18] Andreas Geiger, Philip Lenz, and Raquel Urtasun. Are we ready for autonomous driving? the KITTI vision benchmark suite. In *Proc. IEEE/CVF Conference on Computer Vision and Pattern Recognition (CVPR)*, pages 3354–3361, 2012. 1, 2
- [19] Shirsendu Sukanta Halder, Jean-François Lalonde, and Raoul de Charette. Physics-based rendering for improving robustness to rain. In *Proc. IEEE/CVF Conference on Computer Vision and Pattern Recognition (CVPR)*, pages 10203–10212, 2019. 3
- [20] Matthias Hein and Maksym Andriushchenko. Formal guarantees on the robustness of a classifier against adversarial manipulation. In *Advances in Neural Information Processing Systems (NeurIPS)*. Curran Associates, Inc., 2017. 4
- [21] Dan Hendrycks and Thomas Dietterich. Benchmarking neural network robustness to common corruptions and perturbations. In *Proc. International Conference on Learning Representations (ICLR)*, pages 1–16, 2019. 2, 3
- [22] Alain Hore and Djemel Ziou. Image quality metrics: PSNR vs. SSIM. In *International Conference on Pattern Recognition*, pages 2366–2369. IEEE, 2010. 4
- [23] Zhaoyang Huang, Xiaoyu Shi, Chao Zhang, Qiang Wang, Ka Chun Cheung, Hongwei Qin, Jifeng Dai, and Hongsheng Li. Flowformer: A transformer architecture for optical flow. In *Proc. European Conference on Computer Vision (ECCV)*, pages 668–685. Springer, 2022. 2, 5
- [24] Eddy Ilg, Nikolaus Mayer, Tonmoy Saikia, Margret Keuper, Alexey Dosovitskiy, and Thomas Brox. FlowNet 2.0: Evolution of optical flow estimation with deep networks. In *Proceedings of the IEEE conference on computer vision and pattern recognition*, pages 2462–2470, 2017. 5
- [25] John Immerkaer. Fast noise variance estimation. pages 300–302. Elsevier, 1996. 8
- [26] Azin Jahedi, Maximilian Luz, Lukas Mehl, Marc Rivinius, and Andrés Bruhn. High resolution multi-scale RAFT (Robust Vision Challenge 2022). In *arXiv preprint 2210.16900*. arXiv, 2022. 3, 5
- [27] Azin Jahedi, Lukas Mehl, Marc Rivinius, and Andrés Bruhn. Multi-scale RAFT: Combining hierarchical concepts for learning-based optical flow estimation. In *Proc. IEEE International Conference on Image Processing (ICIP)*, pages 1236–1240, 2022. 3, 5
- [28] Shihao Jiang, Dylan Campbell, Yao Lu, Hongdong Li, and Richard Hartley. Learning to estimate hidden motions with global motion aggregation. In *Proc. IEEE/CVF International Conference on Computer Vision (ICCV)*, pages 9772–9781, 2021. 5
- [29] Steffen Jung, Jovita Lukasik, and Margret Keuper. Neural architecture design and robustness: A dataset. In *Proc. International Conference on Learning Representations (ICLR)*. OpenReview. net, 2023. 2
- [30] Öğuzhan Fatih Kar, Teresa Yeo, Andrei Atanov, and Amir Zamir. 3D common corruptions and data augmentation. In *Proc. IEEE/CVF Conference on Computer Vision and Pattern Recognition (CVPR)*, pages 18963–18974, 2022. 2, 3
- [31] Daniel Kondermann, Rahul Nair, Katrin Honauer, Karsten Krispin, Jonas Andrulis, Alexander Brock, Burkhard Gussefeld, Mohsen Rahimimoghaddam, Sabine Hofmann, Claus Brenner, et al. The HCI benchmark suite: Stereo and flow ground truth with uncertainties for urban autonomous driving. In *Proc. IEEE/CVF Conference on Computer Vision and Pattern Recognition Workshops (CVPRW)*, pages 19–28, 2016. 2
- [32] Lingdong Kong, Youquan Liu, Xin Li, Runnan Chen, Wenwei Zhang, Jiawei Ren, Liang Pan, Kai Chen, and Ziwei Liu. Robo3D: Towards robust and reliable 3d perception against corruptions. In *Proc. IEEE/CVF International Conference on Computer Vision (ICCV)*, pages 19994–20006, 2023. 2, 3
- [33] Tom Koren, Lior Talker, Michael Dinerstein, and Ran Vitek. Consistent semantic attacks on optical flow. In *Proc. Asian Conference on Computer Vision (ACCV)*, pages 1658–1674, 2022. 2
- [34] Lorenzo Lamberti, Lorenzo Bellone, Luka Macan, Enrico Natalizio, Francesco Conti, Daniele Palossi, and Luca Benini. Distilling tiny and ultra-fast deep neural networks for autonomous navigation on nano-uavs. *IEEE Internet of Things Journal*, 2024. 1
- [35] Yijin Li, Yichen Shen, Zhaoyang Huang, Shuo Chen, Weikang Bian, Xiaoyu Shi, Fu-Yun Wang, Keqiang Sun, Hujun Bao, Zhaopeng Cui, Guofeng Zhang, and Hongsheng Li. BlinkVision: A benchmark for optical flow, scene flow and point tracking estimation using rgb frames and events, 2024. 2
- [36] Lahav Lipson, Zachary Teed, and Jia Deng. Raft-stereo: Multilevel recurrent field transforms for stereo matching. In *2021 International Conference on 3D Vision (3DV)*, pages 218–227. IEEE, 2021. 2, 5
- [37] K. T. Yaras Mahima, Asanka G. Perera, Sreenatha Anavatti, and Matt Garratt. FlowCraft: Unveiling adversarial robustness of LiDAR scene flow estimation. 2025. 2
- [38] Daniel Maurer, Nico Marniok, Bastian Goldluecke, and Andrés Bruhn. Structure-from-motion-aware patchmatch for adaptive optical flow estimation. In *Proc. European Conference on Computer Vision (ECCV)*, pages 565–581, 2018. 1
- [39] Nikolaus Mayer, Eddy Ilg, Philip Hausser, Philipp Fischer, Daniel Cremers, Alexey Dosovitskiy, and Thomas Brox. A large dataset to train convolutional networks for disparity, optical flow, and scene flow estimation. In *Proc. IEEE/CVF Conference on Computer Vision and Pattern Recognition (CVPR)*, pages 4040–4048, 2016. 2

- [40] Kimberly McGuire, Guido De Croon, Christophe De Wagter, Karl Tuyls, and Hilbert Kappen. Efficient optical flow and stereo vision for velocity estimation and obstacle avoidance on an autonomous pocket drone. *IEEE Robotics and Automation Letters*, 2(2):1070–1076, 2017. 1
- [41] Morgan McGuire and Louis Bavoil. Weighted blended order-independent transparency. *Journal of Computer Graphics Techniques (JCGT)*, 2013. 3
- [42] Lukas Mehl, Azin Jahedi, Jenny Schmalfuss, and Andrés Bruhn. M-fuse: Multi-frame fusion for scene flow estimation. In *Proc. IEEE/CVF Winter Conference on Applications of Computer Vision (WACV)*, pages 2020–2029, 2023. 2, 4, 5, 3
- [43] Lukas Mehl, Jenny Schmalfuss, Azin Jahedi, Yaroslava Naliyayko, and Andrés Bruhn. Spring: A high-resolution high-detail dataset and benchmark for scene flow, optical flow and stereo. In *Proc. IEEE/CVF Conference on Computer Vision and Pattern Recognition (CVPR)*, pages 4981–4991, 2023. 1, 2, 5
- [44] Lukas Mehl, Andrés Bruhn, Markus Gross, and Christopher Schroers. Stereo conversion with disparity-aware warping, compositing and inpainting. In *Proc. IEEE/CVF Winter Conference on Applications of Computer Vision (WACV)*, pages 4260–4269, 2024. 1
- [45] Moritz Menze and Andreas Geiger. Object scene flow for autonomous vehicles. In *Proc. IEEE/CVF Conference on Computer Vision and Pattern Recognition (CVPR)*, pages 3061–3070, 2015. 1, 2, 8
- [46] Claudio Michaelis, Benjamin Mitzkus, Robert Geirhos, Evgenia Rusak, Oliver Bringmann, Akexander S. Ecker, Matthias Bethge, and Wieland Brendel. Benchmarking robustness in object detection: Autonomous driving when winter is coming. In *Proc. Conference on Neural Information Processing Systems Workshops (NeurIPS W)*, 2019. 2, 3
- [47] Sergiu Mocanu, Alan R Moody, and April Khademi. FlowReg: fast deformable unsupervised medical image registration using optical flow. *Journal of Machine Learning for Biomedical Imaging (MELBA)*, 2021. 1
- [48] Patrick Müller, Alexander Braun, and Margret Keuper. Classification robustness to common optical aberrations. In *Proc. IEEE/CVF International Conference on Computer Vision Workshops (ICCVW)*, pages 3632–3643, 2023. 2, 3
- [49] Patricia Pauli, Anne Koch, Julian Berberich, Paul Kohler, and Frank Allgöwer. Training robust neural networks using lipschitz bounds. In *IEEE Control Systems Letters*, pages 121–126, 2022. 4
- [50] Tan-Binh Phan, Dinh-Hoan Trinh, Didier Wolf, and Christian Daul. Optical flow-based structure-from-motion for the reconstruction of epithelial surfaces. *Pattern Recognition (PR)*, 2020. 1
- [51] Markus Philipp, Neal Bacher, Stefan Saur, Franziska Mathis-Ullrich, and Andrés Bruhn. From chairs to brains: customizing optical flow for surgical activity localization. In *IEEE International Symposium on Biomedical Imaging (ISBI)*, 2022. 1
- [52] Anurag Ranjan and Michael J Black. Optical flow estimation using a spatial pyramid network. In *Proc. IEEE/CVF Conference on Computer Vision and Pattern Recognition (CVPR)*, pages 4161–4170, 2017. 5
- [53] Anurag Ranjan, Joel Janai, Andreas Geiger, and Michael J. Black. Attacking optical flow. In *Proc. IEEE/CVF International Conference on Computer Vision (ICCV)*, pages 2004–2013, 2019. 2, 4
- [54] Anurag Ranjan, David T. Hoffmann, Dimitrios Tzionas, Siyu Tang, Javier Romero, and Michael J. Black. Learning multi-human optical flow. *International Journal of Computer Vision (IJCV)*, 128(4):873–890, 2020. 2
- [55] Stephan Richter, Zeeshan Hayder, and Vladlen Koltun. Playing for benchmarks. In *Proc. IEEE/CVF International Conference on Computer Vision (ICCV)*, pages 2232–2241, 2017. 1, 2
- [56] Benoît Rosa, Valentin Bordoux, and Florent Nageotte. Combining differential kinematics and optical flow for automatic labeling of continuum robots in minimally invasive surgery. *Frontiers in Robotics and AI*, 6:86, 2019. 1
- [57] Daniel Scharstein, Heiko Hirschmüller, York Kitajima, Greg Krathwohl, Nera Nesić, Xi Wang, and Porter Westling. High-resolution stereo datasets with subpixel-accurate ground truth. In *Proc. German Conference on Pattern Recognition (GCPR)*, 2014. 1, 2
- [58] Erik Scheurer, Jenny Schmalfuss, Alexander Lis, and Andrés Bruhn. Detection defenses: An empty promise against adversarial patch attacks on optical flow. In *Proc. IEEE/CVF Winter Conference on Applications of Computer Vision (WACV)*, pages 6489–6498, 2024. 2
- [59] Jenny Schmalfuss, Lukas Mehl, and Andrés Bruhn. Attacking motion estimation with adversarial snow. *ECCV 2022 Workshop on Adversarial Robustness in the Real World (ECCV-AROW)*, 2022. 2, 4
- [60] Jenny Schmalfuss, Philipp Scholze, and Andrés Bruhn. A perturbation-constrained adversarial attack for evaluating the robustness of optical flow. In *Proc. European Conference on Computer Vision (ECCV)*, pages 183–200, 2022. 1, 2, 4, 6
- [61] Jenny Schmalfuss, Lukas Mehl, and Andrés Bruhn. Distracting downpour: Adversarial weather attacks for motion estimation. In *Proc. IEEE/CVF International Conference on Computer Vision (ICCV)*, pages 10106–10116, 2023. 2, 3, 4
- [62] Thomas Schöps, Johannes L. Schönberger, Silvano Galliani, Torsten Sattler, Konrad Schindler, Marc Pollefeys, and Andreas Geiger. A multi-view stereo benchmark with high-resolution images and multi-camera videos. In *Proc. IEEE/CVF Conference on Computer Vision and Pattern Recognition (CVPR)*, 2017. 1, 2
- [63] Simon Schrodin, Tonmoy Saikia, and Thomas Brox. Towards understanding adversarial robustness of optical flow networks. In *Proc. IEEE/CVF Conference on Computer Vision and Pattern Recognition (CVPR)*, pages 8916–8924, 2022. 2
- [64] Markus Schulze. The schulze method of voting. *arXiv preprint arXiv:1804.02973*, 2018. 5
- [65] Deqing Sun, Xiaodong Yang, Ming-Yu Liu, and Jan Kautz. PWC-Net: CNNs for optical flow using pyramid, warping, and cost volume. In *Proc. IEEE/CVF Conference on Computer Vision and Pattern Recognition (CVPR)*, 2018. 5

- [66] Deqing Sun, Daniel Vlasic, Charles Herrmann, Varun Jampani, Michael Krainin, Huiwen Chang, Ramin Zabih, William T. Freeman, , and Ce Liu. AutoFlow: Learning a better training set for optical flow. In *Proc. IEEE/CVF Conference on Computer Vision and Pattern Recognition (CVPR)*, 2021. 2
- [67] Shiyu Tang, Ruihao Gong, Yan Wang, Aishan Liu, Jiakai Wang, Xinyun Chen, Fengwei Yu, Xianglong Liu, Dawn Song, Alan Yuille, Philip H.S. Torr, and Dacheng Tao. RobustART: Benchmarking robustness on architecture design and training techniques. <https://arxiv.org/pdf/2109.05211.pdf>, 2021. 2
- [68] Rohan Taori, Achal Dave, Vaishaal Shankar, Nicholas Carlini, Benjamin Recht, and Ludwig Schmidt. Measuring robustness to natural distribution shifts in image classification. pages 18583–18599. Curran Associates, Inc., 2020. 2, 4
- [69] Zachary Teed and Jia Deng. RAFT: Recurrent all-pairs field transforms for optical flow. In *Proc. European Conference on Computer Vision (ECCV)*, pages 402–419, 2020. 2, 4, 5, 3
- [70] Zachary Teed and Jia Deng. RAFT-3D: Scene flow using rigid-motion embeddings. In *Proceedings of the IEEE/CVF conference on computer vision and pattern recognition*, pages 8375–8384, 2021. 2, 5
- [71] Dimitris Tsipras, Shibani Santurkar, Logan Engstrom, Alexander Turner, and Aleksander Madry. Robustness may be at odds with accuracy. In *International Conference on Learning Representations (ICLR)*, 2019. 1, 2, 4, 5
- [72] Pengfei Wang, Xiaofei Hui, Beijia Lu, Nimrod Lilith, Jun Liu, and Sameer Alam. Left-right discrepancy for adversarial attack on stereo networks, 2024. 2
- [73] Thomas Wiesemann and Xiaoyi Jiang. Fog augmentation of road images for performance analysis of traffic sign detection algorithms. In *Proc. International Conference on Advanced Concepts for Intelligent Vision Systems (ACVIS)*, 2016. 3
- [74] Alex Wong, Mukund Mundhra, and Stefano Soatto. Stereopagnosia: Fooling stereo networks with adversarial perturbations. *Proc. AAAI Conference on Artificial Intelligence (AAAI)*, pages 2879–2888, 2021. 2
- [75] Gangwei Xu, Junda Cheng, Peng Guo, and Xin Yang. Attention concatenation volume for accurate and efficient stereo matching. In *Proceedings of the IEEE/CVF conference on computer vision and pattern recognition*, pages 12981–12990, 2022. 5
- [76] Haofei Xu, Jing Zhang, Jianfei Cai, Hamid Rezaatofighi, and Dacheng Tao. Gmflow: Learning optical flow via global matching. In *Proc. IEEE/CVF Conference on Computer Vision and Pattern Recognition (CVPR)*, pages 8121–8130, 2022. 2, 5
- [77] Koichiro Yamanaka, Keita Takahashi, Toshiaki Fujii, and Ryuraro Matsumoto. Simultaneous attack on CNN-based monocular depth estimation and optical flow estimation. *IEICE Transactions on Information and Systems*, pages 785–788, 2021. 2
- [78] Zhonghua Yi, Hao Shi, Qi Jiang, Yao Gao, Ze Wang, Yufan Zhang, Kailun Yang, and Kaiwei Wang. Benchmarking the robustness of optical flow estimation to corruptions, 2024. 2
- [79] Feihu Zhang, Victor Prisacariu, Ruigang Yang, and Philip HS Torr. Ga-net: Guided aggregation net for end-to-end stereo matching. In *Proceedings of the IEEE/CVF conference on computer vision and pattern recognition*, pages 185–194, 2019. 5
- [80] Qingwen Zhang, Yi Yang, Peizheng Li, Olov Andersson, and Patric Jensfelt. Seflow: A self-supervised scene flow method in autonomous driving. In *Proc. European Conference on Computer Vision (ECCV)*, pages 353–369, 2025. 1
- [81] Yuanhang Zheng, Harald Köstler, Nils Thürey, and Ulrich Rüde. Enhanced motion blur calculation with optical flow. In *Proc. Workshop on Vision, Modeling and Visualization (VMV)*, 2006. 3
- [82] Yinqiang Zheng, Mingfang Zhang, and Feng Lu. Optical flow in the dark. In *Proc. IEEE/CVF Conference on Computer Vision and Pattern Recognition (CVPR)*, 2020. 2